Inhibition of p38-MK2 pathway enhances the efficacy of microtubule inhibitors in breast cancer cells

Yu-Chia Chen[1, 2, 7], Mamoru Takada[3, 7], Aerica Nagornyuk[4], Wu Muhan[3], Hideyuki Yamada[3], Takeshi Nagashima[3], Masayuki Ohtsuka[3], Jennifer G. DeLuca[5], Steven Markus[5], Motoki Takaku[4], & Aussie Suzuki[1, 2, 6, 8]

1. McArdle Laboratory for Cancer Research, Department of Oncology, University of Wisconsin-Madison, Madison, Wisconsin, USA
2. Molecular Cellular Pharmacology Graduate Program, University of Wisconsin-Madison, Madison, Wisconsin, USA
3. Department of General Surgery, Graduate School of Medicine, Chiba University, Chiba, Japan
4. Department of Biomedical Science, University of North Dakota School of Medicine and Health Science, Grand Folks, North Dakota, USA
5. Department of Biochemistry and Molecular Biology, Colorado State University, Fort Collins, Colorado, USA
6. Carbone Comprehensive Cancer Center, University of Wisconsin-Madison, Madison, Wisconsin, USA
7. These authors contributed equally
8. Corresponding (aussie.suzuki@wisc.edu)

Competing Interest Statement: The authors declare no potential conflicts of interest.

Abstract

Microtubule-targeting agents (MTAs) have been successfully translated from basic research into clinical therapies and have been widely used as first- and second-line chemotherapy drugs for various cancers. However, current MTAs exhibit positive responses only in subsets of patients and are often accompanied by side effects due to their impact on normal cells. This underscores an urgent need to develop novel therapeutic strategies that enhance MTA efficacy while minimizing toxicity to normal tissues. In this study, we demonstrate that inhibition of the p38-MK2 (MAP kinase-activated protein kinase 2) pathway sensitizes cancer cells to MTA treatment. We utilize CMPD1, a dual-target inhibitor, to concurrently suppress the p38-MK2 pathway and microtubule dynamicity. In addition to established role as an MK2 inhibitor, we find that CMPD1 rapidly induces microtubule depolymerization, preferentially at the microtubule plus-end, leading to the inhibition of tumor growth and cancer cell invasion in both *in vitro* and *in vivo* models. Notably, 10 nM CMPD1 is sufficient to induce irreversible mitotic defects in cancer cells, but not in non-transformed RPE1 cells, highlighting its high specificity to cancer cells. We further validate that a specific p38-MK2 inhibitor significantly potentiates the efficacy of sub-clinical concentrations of MTA. In summary, our findings suggest that the p38-MK2 pathway presents a promising therapeutic target in combination with MTAs in cancer treatment.

Introduction

Cancer, a disease characterized by uncontrolled cell growth, results from cells that proliferate indefinitely without external growth signals[1, 2]. Consequently, targeting cell cycle progression is a powerful therapeutic strategy for cancer treatment[3, 4]. Microtubule-targeting agents (MTAs) disrupt spindle microtubule assembly during mitosis, making them widely-used chemotherapy drugs for various tumors[5-7]. By impairing microtubule dynamics and functions, MTAs activate the spindle assembly checkpoint (SAC)[8-10], leading to mitotic arrest, mitotic defects, and apoptotic cell death[5, 11]. MTAs are functionally categorized into two groups: microtubule stabilizers (e.g., taxanes)[12, 13] and microtubule depolymerizers (e.g., eribulin)[14, 15]. Paclitaxel (PTX), a taxane, has been a highly successful anti-cancer drug in clinical use for over 30 years[12, 16]. However, several limitations hinder its therapeutic efficacy. Firstly, only a subset of breast and ovarian cancer patients exhibit a favorable response to PTX[17-19]. Secondly, PTX lacks tumor specificity, leading to off-target effects, including neutropenia, gastrointestinal disorders, and peripheral neuropathy[20-24]. Thirdly, cancer cells can acquire resistance to PTX through mechanisms such as the upregulation of drug efflux proteins (e.g., P-glycoprotein) or class III β-tubulin, which reduces PTX binding affinity[25-27]. In contrast, eribulin, a second-line chemotherapeutic agent, has a lower incidence of peripheral neuropathy, one of the most troublesome side effect of MTAs[28]. Due to its distinct mechanism of action, eribulin is effective against taxane-resistant tumors[29-32]. However, clinical studies have demonstrated that fewer than 20% of metastatic breast

cancer patients, previously treated with chemotherapy, respond positively to eribulin[33, 34]. MTAs remain central to the treatment of breast and ovarian cancers, including metastatic cases. Therefore, developing new strategies to overcome the limitations associated with MTAs is critical for optimizing therapeutic outcomes in cancer treatment.

The p38 mitogen-activated protein kinase (MAPK) signaling pathway, activated by a variety of environmental and intracellular stimuli[35-38], plays a crucial role in numerous biological processes, including DNA repair, inflammation, cell differentiation, and cell death[39-44]. MAPK-activated protein kinase 2 (MK2) is a major downstream substrate of p38 MAPK[45]. Previous studies have shown that phosphorylated MK2 localizes to mitotic spindles, and that MK2 depletion leads to abnormal spindle formation, defects in chromosome alignment, and mitotic arrest in both human cells and mouse oocytes, indicating a vital role of MK2 in mitotic progression[46, 47]. CMPD1 was originally developed as a selective inhibitor targeting the p38-dependent phosphorylation of MK2 (**Fig. 1A**)[48-51]. Subsequent studies revealed that CMPD1 could induce G2/M arrest in glioblastoma and gastric cancer cells, as observed by flow cytometry[52, 53], and suggested its potential role in inhibiting microtubule polymerization *in vitro*[53]. However, the precise and dynamic nature of CMPD1's effects on microtubule dynamics and cancer cell proliferation have yet to be fully elucidated. In this study, we demonstrate that CMPD1 preferentially induces severe mitotic defects in breast cancer cells and effectively inhibits cancer cell growth, migration, and invasion in both *in vitro* and *in vivo* models. Notably, CMPD1 uniquely triggers rapid

microtubule depolymerization at the plus-end *in vitro*. These results indicate that the inhibition of p38-MK2 pathway could enhance the therapeutic efficacy of MTAs. We validate this hypothesis by demonstrating that a specific MK2 inhibitor, MK2-IN-3, in combination with vinblastine, a clinically approved microtubule destabilizer[54, 55], exhibits significantly increased efficacy in inducing mitotic defects. Thus, our results suggest that the p38-MK2 pathway may serve as a promising therapeutic target in combination with MTAs in cancer treatment.

Results

CMPD1 induces robust prometaphase arrest in breast cancer cell lines

Cell cycle inhibitors, particularly MTAs, are standard chemotherapy drugs for breast cancer[54]. To investigate whether CMPD1 induces G2/M arrest in breast cancer cells, we treated MDA-MB-231 cells, a triple-negative breast cancer (TNBC) cell line, with varying concentrations of CMPD1 and analyzed its effects on cell cycle progression using flow cytometry. The results demonstrated that CMPD1 effectively arrested MDA-MB-231 cells in the G2/M phase at concentrations ranging from 1 to 10 μM (**Fig. 1B**), consistent with previous observations in glioblastoma cells[53]. Given that flow cytometry cannot distinguish between G2 phase and mitosis, we performed high-temporal resolution live-cell imaging to further dissect the impact of CMPD1 on cell cycle progression across various breast cancer cell lines, including MDA-MB-231 (TNBC), CAL-51 (TNBC), and T-47D (luminal A)[56, 57]. Our

findings revealed that CMPD1 induced a severe prometaphase arrest across all tested breast cancer cell lines, regardless of subtypes, with most cells remaining arrested in prometaphase for over 10 hours, while control cells divided within 30-60 min (**Fig. 1C-D** and **Supplementary Movies 1-2**). Since CAL-51 cells harbor wild-type TP53, whereas the other two cell lines do not[58, 59], these results suggest that CMPD1 induces a robust prometaphase arrest in breast cancer cells through a p53-independent mechanism.

Breast cancer cells exhibit heightened sensitivity to CMPD1 treatment compared to normal cells.

We demonstrated that concentrations exceeding 1 μM of CMPD1 effectively induced a robust prometaphase arrest in multiple breast cancer cell lines (**Fig. 1D**). In contrast, recent studies on MTA treatment for breast cancer have identified that the clinically relevant concentration of PTX in tissue culture cells ranges from 5 to 50 nM[60]. Within this range of concentration, PTX does not induce severe mitotic arrest as observed at higher concentrations (> 1 μM), but it significantly increases the incidence of mitotic errors, thereby promoting chromosomal instability (CIN) and ultimately leading to cancer cell death[60]. Given these findings, we next explored whether sub-μM concentrations of CMPD1 could induce CIN in breast cancer cells. To this end, we treated MDA-MB-231 and CAL-51 cells, along with RPE1 non-transformed retinal pigment epithelial cells (serving as a normal cell control), with either 10 or 50 nM CMPD1. We then compared the impact of

CMPD1 on chromosome segregation using live-cell imaging. In the absence of CMPD1, no significant differences in mitotic duration were observed among RPE1, MDA-MB-231, and CAL-51 cells (**Fig. 2A-C**). However, upon treatment with 10 or 50 nM CMPD1, all cell lines were arrested in prometaphase (**Fig. 2A-C**). Notably, MDA-MB-231 and CAL-51 cells displayed significantly prolonged mitotic duration compared to RPE1 cells (**Fig. 2A-C**), indicating greater sensitivity of breast cancer cells to CMPD1 treatment relative to normal cells. Given that mitotic errors are a direct cause of CIN, we next assessed the frequency of mitotic errors including misaligned chromosome, chromosome bridge, lagging chromosome and multipolar division under these conditions (**Fig. 2D**). Both MDA-MB-231 and CAL-51 cells exhibited a significantly higher rate of mitotic errors when exposed to 10 or 50 nM CMPD1 (**Fig. 2E**). For instance, approximately 90% and 100% of CAL-51 cells experienced mitotic errors in the presence of 10 and 50 nM CMPD1, respectively (**Fig. 2E**). Conversely, nearly 100% of RPE1 cells underwent faithful cell division even at the same concentrations of CMPD1 (**Fig. 2E**). To determine whether CMPD1 selectively targets cancer cells compared to other MTAs, we evaluated mitotic error rates in the same cell lines treated with a clinically relevant concentration of PTX (10 nM). Our results demonstrated that both RPE1 and breast cancer cell lines displayed comparably high rates of mitotic errors when treated with 10 nM PTX treatment (**Fig. 2F**), consistent with previous observations[60]. In summary, unlike PTX, CMPD1 induces CIN with selective toxicity toward breast cancer cells.

To further investigate the selectivity of CMPD1 in breast cancer cells, we conducted a CMPD1 washout assay using the above cell lines, aiming to recapitulate the clinical condition where the concentration of chemotherapy drugs in patients is diluted due to the "drug holiday" between regular treatments. In this assay, we treated the cells with 2 μM CMPD1 for 12 hours, followed by a washout before imaging. We observed that the mitotic duration was significantly prolonged in both MDA-MB-231 and CAL-51 cells upon CMPD1 washout (85 min and 151 min, respectively) compared to RPE1 cells (14 min) (**Fig. 2G-H**). This suggests that breast cancer cells struggle to recover from CMPD1-induced mitotic arrest, whereas normal cells can immediately resume progression to proper anaphase. Notably, 90% and 81% of mitotic cells in MDA-MB-231 and CAL-51 cells lines, respectively, exhibited mitotic errors, whereas 50% of RPE1 cells displayed normal chromosome segregation (**Fig. 2G, I**). These findings reinforce the hypothesis that breast cancer cells are more sensitive to CMPD1 treatment under clinically relevant conditions. Interestingly, approximately 60% of MDA-MB-231 cells that entered mitosis after CMPD1 washout still exhibited mitotic errors, while only ~10% of RPE1 cells showed errors. This suggests a prolonged impact of CMPD1 on mitosis in breast cancer cells (**Fig. S1C**). Consistent with the increased sensitivity in breast cancer cells to CMPD1, MDA-MB-231 cells exhibited a significantly higher frequency of apoptotic cell death during or shortly after mitosis within 24 of CMPD1 washout, compared to RPE1 cells (**Fig. S1D-E**). Collectively, these results underscore that breast cancer cells are more sensitive to CMPD1 treatment than normal

RPE1 cells, particularly in a clinically relevant context.

CMPD1 inhibits anchorage independent growth and tumor growth in mouse xenograft

We subsequently evaluated the efficacy of CMPD1 in inhibiting anchorage-independent growth, a critical hallmark of tumorigenesis, in MDA-MB-231 cells. CMPD1 demonstrated a potent dose-dependent inhibition, with 500 nM being sufficient to completely suppress colony formation (**Fig. 3A-B, Fig. S2A-B**). Remarkably, even at a relatively lower concentration (250 nM), CMPD1 significantly reduced colony formation, surpassing the inhibitory effects of 10 μM PTX. These findings suggest that CMPD1 is more effective than PTX in inhibiting the anchorage-independent growth of MDA-MB-231 cells.

We demonstrated that CMPD1 effectively inhibits cancer cell growth in a tissue culture model. Next, we investigated whether CMPD1 could also inhibit tumor growth *in vivo*. For this purpose, we employed an MDA-MB-231 xenograft mouse model and found that CMPD1 significantly suppressed tumor growth (**Fig. 3C-E**). Notably, while both PTX and CMPD1 suppressed tumor growth in mice, CMPD1 achieved comparable efficacy at concentrations 10-100 times lower than PTX. Furthermore, two mice treated with PTX died during the experiment, whereas all CMPD1-treated mice survived and remained healthy throughout the treatment regimen. (**Fig. S2C**). These findings suggest that CMPD1 is not

only effective in inhibiting tumor growth in both *in vitro* and *in vivo* models but also appears to be more potent and safer than PTX, a standard chemotherapeutic agent for breast cancer treatment.

CMPD1 exhibits a preferential depolymerizing effect on the microtubule plus-end

We demonstrated that at least ≥1 μM CMPD1 induced a robust prometaphase arrest in breast cancer cell lines (**Fig. 1D**). A previous study suggests that CMPD1 may possess the ability to inhibit tubulin polymerization, as indicated by *in vitro* tubulin polymerization assay[53]. To elucidate the mechanism underlying the CMPD1-induced prometaphase arrest, we performed high spatiotemporal resolution live-cell imaging to monitor microtubule dynamics in metaphase CAL-51 cells (see **Methods**). In these cells, α-tubulin and histone H2B genes were endogenously labeled with mNeonGreen and mScarlet, respectively, using CRISPR-Cas9 technology[60]. Our results revealed that the signal intensity of mitotic spindles dramatically decreased to less than 10% within 8 min following CMPD1 treatment. (**Fig. 4A-B** and **Supplementary Movies 3-4**). Concurrently, the formation of multipolar spindle poles was observed (**Fig. 4A**). The decrease in spindle signal intensity correlated with a gradual disruption of the metaphase plate, likely due to the loss of kinetochore-microtubule attachments (**Fig. 4A**). Moreover, we observed that CMPD1-treated cells exited G2 phase and underwent nuclear envelope breakdown (NEBD), even though these cells were unable to assemble mitotic spindles (**Fig. 4C**). This

finding further supports that CMPD1 specifically arrests cells in prometaphase rather than G2 phase. To determine whether CMPD1 induces rapid microtubule depolymerization or the degradation of tubulin proteins, we pre-treated the cells with MG132, a proteasome inhibitor, for 1 hour prior to CMPD1 treatment (**Fig. 4A-B** and **Supplementary movie 5**). We found that proteasome inhibition did not prevent the CMPD1-mediated reduction in spindle signals (**Fig. 4A-B**), suggesting that CMPD1 directly induces microtubule depolymerization in breast cancer cells.

To further investigate the mechanism underlying CMPD1-induced microtubule depolymerization, we conducted TIRF (Total Internal Reflection Fluorescence Microscopy) experiments to observe microtubule behaviors in response to CMPD1 treatment. The conventional TIRF assay utilizing PTX-stabilized immobilized microtubules is widely used due to its ease of use. However, this approach lacks the dynamic nature of microtubules as seen in living cells, limiting the study of CMPD1's effects under more physiological conditions. To overcome this limitation, we utilized GMPCPP-stabilized microtubule seeds combined with rhodamine-labeled tubulin, which allows for the observation of microtubule growth and shrinkage at both ends, thereby better mimicking the dynamic behavior of microtubules in mitotic cells. As expected, microtubules exhibited repeated cycles of growth and shrinkage at both plus and minus ends, with a higher stability at minus ends (**Fig. 4D**). Upon treatment with CMPD1, there was a marked reduction in the proportion of microtubules with plus-end extensions within just 1 min (**Fig. 4D-F**), along with an

increased frequency of microtubule catastrophes, reduced growth rates, and decreased maximum lengths of plus-end extensions (**Fig. 4G-H**). Interestingly, CMPD1's effects on the minus ends of microtubules were notably different. Neither the fraction of microtubules with minus end extensions nor the catastrophe frequency at minus ends were significantly different from control (**Fig. 4D-H**). However, minor reductions were observed in the average maximum length of minus-end extensions and their growth rates (**Fig. 4H**). In contrast, vinblastine, a well-characterized microtubule destabilizer, rapidly depolymerized microtubules from both ends (**Fig. 4D-E**), highlighting that CMPD1 uniquely and preferentially depolymerizes microtubules from the plus ends. Collectively, our cell biology and biochemical data demonstrate that CMPD1 alone can depolymerize microtubules, with a pronounced preference for plus-end depolymerization.

CMPD1 inhibits cell migration and invasion

Since proper microtubule dynamics is essential for regulating cell locomotion[61-63], we hypothesized that the improper microtubule dynamics induced by CMPD1 might inhibit cell migration. To investigate this, we evaluated the migratory capacity of CAL-51 cells using a wound healing assay following treatment with CMPD1. Our findings revealed that CMPD1, at concentrations ranging from 100 nM to 10 µM, significantly inhibited wound closure compared to the control (**Fig. 5A-B**), demonstrating its potential to suppress cancer cell migration and invasion. To further examine this hypothesis, we conducted a

transwell-invasion assay using MDA-MB-231 cells. Treatment with CMPD1 at concentrations greater than 100 nM significantly suppressed breast cancer cell invasion, and at 1 µM, CMPD1 completely abolished this cancer invasion (**Fig. 5C-D**).

To determine whether CMPD1 inhibits cancer cell invasion *in vivo*, we assessed the frequency of invasion of cancer cells into blood vessels by examining the tissue sections of mice with cancer cell-derived xenografts described in **Fig. 3C**. CMPD1-treated mice displayed a significantly reduced frequency of cancer cell-infiltrated vessels compared to vehicle-treated mice, suggesting that CMPD1 significantly inhibits metastasis *in vivo* (**Fig. 5E**). Together, these results show that CMPD1 suppresses cancer cell migration and invasion *in vitro* and *in vivo*.

Inhibiting the p38-MK2 pathway significantly enhances the efficacy of microtubule depolymerizing agents

CMPD1's distinct ability to inhibit tumor growth may stem from its dual inhibitory effect on both the p38-MK2 signaling pathway and microtubule dynamics. To rigorously test the hypothesis that inhibition of the p38-MK2 pathway could potentiate the efficacy of MTAs, we assessed the combinatorial effects of MK2-IN-3 (hereafter referred to as MK2i), a selective MK2 inhibitor, and clinically relevant concentrations of vinblastine (1 or 5 nM) on mitotic progression in CAL-51 cells. Individual treatment with either 10 µM MK2i or 1 nM vinblastine did not significantly alter the frequency of mitotic slippage or mitotic cell death

compared to the control, although both treatments modestly prolonged mitotic duration and increased the frequency of mitotic errors (approximately 2 to 3-fold compared to control) (**Fig. 6A**). Strikingly, the combination of 10 µM MK2i with 1 nM vinblastine resulted in a profound synergistic effect, extending mitotic duration by approximately 13-fold and markedly increasing the frequency of mitotic errors and cell death (**Fig. 6A, Condition 4**). A similar synergistic effect was also observed when cells were simultaneously treated with 10 µM MK2i and 5 nM vinblastine, although the 5 nM vinblastine alone induced a more pronounced mitotic arrest compared to the control and 1 nM vinblastine (**Fig. 6A, Condition 6**). To better understand the impact of CMPD1 treatment on cancer cells at the gene expression level, we conducted RNA-seq analysis. When an FDR < 0.05 was applied using DESeq2 for differential gene expression analysis, 351 genes were found to be up-regulated, and 425 genes were down-regulated 24 hours after treatment with 10 µM CMPD1 (**Fig. 6B**). Gene ontology (GO) biological process (BP) pathway enrichment analysis revealed that the most significantly enriched pathways in up-regulated genes relate to cell migration, while down-regulated genes are predominantly associated with mitosis and chromosome segregation (**Fig. 6C**). To explore whether unique pathways were up- or down-regulated specifically in cancer cells, RNA-seq analysis was also performed on RPE1 cells. Comparing differentially expressed genes between MDA-MB-231 cells and RPE1 cells, cell death and apoptosis pathways were significantly enriched in genes uniquely upregulated in MDA-MB-231 cells (**Fig. 6D**). Genes specifically downregulated in

MDA-MB-231 cells were again enriched in pathways related to mitosis and chromosome segregation (**Fig. 6D**), consistent to the results that cancer cells are more sensitive to CMPD1 treatment (**Fig. 2**). Collectively, CMPD1 upregulates cell death pathways while selectively downregulates mitotic genes in cancer cells, highlighting its potent cancer cell specificity. The pivotal role of the p38-MK2 signaling pathway in enhancing the efficacy of microtubule destabilizers likely contributes to these observed gene expression changes.

Discussion

MTAs have been widely utilized as first- or second-line chemotherapy agents for various cancer; however, MTA-based treatment is often compromised by several limitations, including severe adverse effects and the development of drug resistance[20-24]. Consequently, the development of novel therapeutic strategies to enhance the effectiveness of MTAs remains critical for improving clinical outcomes in cancer patients. In this study, we propose that inhibiting the p38-MK2 pathway can synergize with MTAs to significantly enhance their therapeutic efficacy. We demonstrate this synergistic effect by using a combination of an MK2-specific inhibitor with the microtubule depolymerizer vinblastine, alongside CMPD1, a dual-target inhibitor that simultaneously disrupts both the MK2 signaling pathway and microtubule dynamics (**Fig. 6A**). Our findings reveal that CMPD1 exhibits a unique ability to depolymerize microtubules specifically at their plus-ends, as well as selectively inducing mitotic defects and altering gene expression profiles in cancer cells (**Fig. 2, 4D-H,** and

6B-D). Furthermore, CMPD1 exhibited potency comparable to or greater than PTX in inhibiting tumor growth both *in vitro* and *in vivo* (**Fig. 3**). In terms of tumor specificity, PTX at clinically relevant concentrations lacks cancer selectivity[60], whereas CMPD1, at similar low concentrations, specifically induces mitotic defects in breast cancer cells without affecting mitotic fidelity in non-transformed cells (**Fig. 2**). These findings suggest that p38-MK2 inhibition has the potential to enhance MTA efficacy, allowing for the improved tumor growth inhibition at a lower MTA concentration, thereby reducing the risk of side effects.

To gain a deeper understanding of CMPD1's cancer cell selectivity, we conducted RNA-seq to compare global gene expression profiles between MDA-MB-231 and RPE1 cell lines, both with or without CMPD1 treatment (**Fig. 6B**). CMPD1 treatment selectively up-regulated gene pathways associated with cell death, aligning with its observed higher cytotoxicity to cancer cells. The cancer-specific selectivity of CMPD1 may also be attributed to differential expression levels of p38 and MK2. Previous studies have reported that MK2 is overexpressed in multiple myeloma (MM) and has a potential to serve as a marker of poor prognosis[64, 65]. Since MK2 facilitates the proliferation of MM cells by activating the Akt signaling pathway, depletion or inhibition of MK2 significantly impairs the growth of MM cells[64, 65]. Furthermore, p38, MK2, and phospho-MK2 are markedly upregulated in primary tumors of various cancers and exhibit an inverse correlation with overall survival rates[66-70]. Therefore, cancer cells with elevated MK2 or phospho-MK2 expression are likely more sensitive to treatments involving MK2 inhibitors. However, further studies are required to

elucidate the detailed molecular mechanisms by which MK2 inhibitors enhance the efficacy of MTAs. Our study has demonstrated synergistic effects between MK2 inhibitors and MTAs, suggesting that the p38-MK2 pathway represents a promising therapeutic target in combination with MTAs for cancer chemotherapy.

Acknowledgements

We thank Drs. Most S. Parvin, Ainslie Homan, Ozge Ali, Masaharu Kasuya, Wang Junchiao, Randy Owen, and Alex Li for help to part of data and image analysis. Part of this work is supported by Wisconsin Partnership Program, Research Forward from VCRGE, start-up funding from University of Wisconsin-Madison SMPH, UW Carbone Cancer Center, and McArdle Laboratory for Cancer Research, and NIH grant R35GM147525 (to A.S.), NIH P20GM104360 and UND School of Medicine & Health Sciences Dean's fund (to M. Takaku), JSPS KAKENHI 21K08638 (to M. Takada), R35GM130365 and NSF NSF1518083 (to J. G. DeLuca), and R35GM139483 and NSF1518083 (to S. Markus).

Author Contributions: Y. Chen. performed most cell biology experiments and data analysis with guidance by A. Suzuki. M. Takada, W. Muhan, H. Yamada, T. Nagashima, and M. Ohtuka performed mouse xenograft experiments, invasion assay, and data analysis. M. Takada, A. Nagornyuk. and M. Takaku performed RNAseq experiments and data analysis. J. G. DeLuca and S. Markus performed in vitro microtubule dynamics experiments and data analysis. A. Suzuki conceptualized and supervised the entire project. M. Takada designed details of xenograft and invasion assay and oversaw the experiments conducted

by H. Muhan, H. Yamada. A. Suzuki and Y. Chen drafted the manuscript, and M. Takada, S. Markus, J. G. DeLuca, and M. Takaku edited manuscript. All authors revised and contributed to the manuscript.

Materials and Methods

Cell Culture

RPE1, CAL-51, MDA-MB-231, T47-D, and HeLa cells were grown in Dulbecco's modified Eagle's medium (DMEM; Gibco) or DMEM/F12 supplemented with 10% FBS (Sigma), 100U/ml penicillin, and 100 mg/ml streptomycin (Gibco) at 37 ˚˙C in a humid atmosphere with 5% CO_2. CMPD1 (Abcam), Taxol (Sigma), MG132 (Sigma), and MPS1 inhibitor (SIGMA, AZ3146) were dissolved in DMSO (Sigma). For washout assay, cells were incubated with 2 µM CMPD1 for 4 hours, then washed by pre-warmed complete media for four times before starting live cell imaging. For cell migration analysis in Figure 5A, cells were grown on iBidi µ-Slide VI for one day. Prior to imaging, cells were twice rinsed by medium without FBS, and then added media containing 15% FBS in only one side to make nutrition gradient (see cartoon diagram in fig. S4A).

Imaging

For time lapse image acquisition, 3D stacked images were obtained sequentially with 1 µm or 3 µm z steps for 12~15 µm total to cover entire mitotic cells using Nikon Elements

software and a high-resolution Nikon Ti-2 inverted microscope equipped with a high-resolution Hamamatsu Flash V2 CMOS camera. The following objectives were used with above scope; 20x (NA 0.75 air), 40x (NA 1.25 silicon, for microtubule depolymerization in a cell), 60x (NA 1.4 oil), 100x (NA 1.4 oil). Images were takes by every 2 or 3 min interval for 24~72 hrs. Cells were grown on glass bottom dish with #1.5 coverslips and incubated in a Tokai Hit STX stage top incubator with PureBox Shiraito clean box (Tokai Hit). Feed-back control of Tokai Hit stage top incubator was used to stably maintain 37 ˚C at growth medium. All imaging was replicated at least three times. For fixed immunofluorescence experiments, cells were grown on high-precision #1.5 coverslips and imaged by a Nikon Ti-2 equipped with a Yokogawa SCU-W1-SoRa spinning disc confocal, Uniformizer, and a Hamamatsu Flash V3 CMOS camera. Quantitative image analysis was performed with Nikon Element (Nikon), MetaMorph (Molecular Devices), and Imaris (Bitplane) (See details in Image analysis section). No post-image processing was performed in all images. All imaging was replicated at least two to four times.

Image analysis

Mitotic durations were measured time between NEBD and anaphase onset or mitotic exit if cells did not exhibit anaphase onset such as CMPD1 treated cells. Histone H2B-EGFP or -mScarlet/RFP was used for determination of mitotic stages. Those images were analyzed using Nikon Element. Tubulin signal intensities on the spindle were

measured using intensities in the custom ROI (region of interest). ROI was drawn onto entire cells in tubulin images, then additional ROI was drawn in cytoplasmic, which is avoided spindles. Second ROI was used for background correction. Similar equation was used in our previous study. Briefly, the integrated intensities from both ROIs were obtained, then the intensity of second ROI was divided by area and times the area of entire cells (first ROI). This value was used for corrections of background for the first ROI. For kinetochore signal measurement in Figure 2B, Integrated fluorescence intensity (minus local background (BG)) measurements were obtained for kinetochores as described previously[71]. A 13 x 13 pixel region was centered on a fluorescent kinetochore to obtain integrated fluorescence, whereas a 15 x 15 pixel region centered on the 13 x 13 pixel region was used to obtain surrounding BG intensity. Measured values were calculated by: Fi (integrated fluorescence intensity minus BG) = integrated intensity for 13 x 13 region – (integrated intensity for the 15 x 15 – integrated intensity for 13 x 13) x pixel area of the 13 x 13 / (pixel area of the 15 x 15 region – pixel area of a 13 x 13 region). Measurements were made with Metamorph 7.7 software (Molecular Devices) using Region Measurements[71]. At least two or three independent replicates of measurements were performed. For cell migration and mobility analysis in Figure 5A-B, we obtained the center of nucleus by particle detection module in Imaris software (Oxford Instrument). The mobility or migration was tracked overtime and then the total length, displacements, and speed were also obtained by Imaris software.

***In vitro* microtubule dynamics assays.**

Microtubules nucleated from GMPCPP-stabilized seeds were prepared and imaged as follows. A microtubule seed mixture was assembled from 50 µM tubulin (7:1:2, unlabeled:488-labeled: biotin-labeled) in BRB80 (80 mM PIPES, 1 mM $MgCl_2$, 1 mM EGTA, pH 6.9), clarified by centrifugation at 90K rpm for 10 min, divided into 2 µl aliquots, snap-frozen in liquid nitrogen, and stored at -80ºC. On the day of imaging, one of these aliquots was thawed, and to this, 0.4 µl 10 mM GMPCPP (Jena Biosciences; 1 mM final) and 1.6 µl BRB80 were added to bring the tubulin to a final concentration of 20 µM. The reaction was incubated at 37ºC for 10 minutes (to promote polymerization) and stored at room temperature for up to 1 day. To prepare for an imaging session, 1 µl of the polymerized biotinylated-seed mixture was diluted 100X (to 200 nM final) into 79 µl BRB80 and 20 µl 0.75% methylcellulose (dissolved in BRB80), both at room temperature (the mixture was pipetted up and down to sheer seeds into smaller sizes). Flow chambers (~4-6 µl in volume) were assembled by adhering plasma-cleaned and biotin/PEGylated glass coverslips (as described in Chandradoss et al., 2014; PMID 24797261) to glass slides using double-stick tape. Streptavidin (0.1 mg/ml; in BRB80) was introduced into the imaging chamber, after which the chamber was incubated at room temperature for 2-10 minutes. The chamber was washed with 10 µl BRB80 supplemented with 1% Pluronic and incubated for ~10-30 seconds, after which 10 µl of the diluted biotinylated-seed mixture was

introduced. The imaging chamber was then immediately placed on a microscope stage prewarmed to 37ºC to monitor seed density in the chamber (we did our best to ensure each chamber had a similar density of seeds). Chambers were washed with 10 µl BRB80 supplemented with 1% Pluronic.

For the polymerization mix, a stock solution of 50 µM tubulin (12.5:1, unlabeled: rhodamine-labeled tubulin) in BRB80 was prepared, clarified by centrifugation at 90K rpm for 10 min, divided into 20 µl aliquots, snap frozen in liquid nitrogen, and stored at -80ºC. Immediately prior to imaging, one of these aliquots was thawed and placed on ice. A 10 µl polymerization mix (final tubulin concentration, 15 µM) was assembled using the following: 3 µl 50 µM tubulin (from above), 0.5 µl 20 mM GTP, 0.5 µl 20 mM b-mercaptoethanol, 2 µl 0.75% methylcellulose, 0.5 µl glucose oxidase/catalase mix (1.2 mg glucose oxidase + 28.1 µl catalase + 99.1 µl BRB80)**,** 0.5 µl 30% glucose,1 µl casein (from a 5% stock of Alkali-soluble Casein), and either 2 µL BRB80 or 2 µl of appropriate drug solution (20 µM CMPD1, or 5 µM vinblastine, each of which was prepared in BRB80). Note that all reagents were prepared or diluted in BRB80. The solution was gently mixed, warmed slightly between gloved fingertips for 10-20 sec, and then immediately added to the flow chamber with the adhered GMPCPP-stabilized microtubule seeds (as described above). Chambers were then incubated for 15 minutes on the microscope state at 37ºC (to approach steady-state), after which a freshly prepared polymerization mix with either tubulin only, or tubulin and a drug was added to the chamber and imaged for 15-20 minutes. For

experiments in which a drug was added mid-way through the imaging period (see kymographs in Figure 2E), we did the following: after the initial 15-minute incubation with tubulin only, a fresh polymerization mix without drug was added, and a 20-minute movie was initiated. After 10 minutes, the movie was briefly paused during which another freshly prepared polymerization mix with drug (or tubulin only) was added to the chamber, and the acquisition was then continued.

Microtubule dynamics were imaged using total internal reflection fluorescence (TIRF) microscopy on an inverted Nikon Ti-E using a 1.49 NA 100X objective equipped with a Ti-S-E motorized stage (Nikon), piezo Z-control (Physik Instrumente), a motorized filter cube turret, a stage-top incubation system (LiveCell, Pathology Devices), and an iXon X3 DU897 cooled EM-CCD camera (Andor). We used 488 nm and 561 nm lasers (Nikon), a multi-pass quad filter cube set (C-TIRF for 405 nm/488 nm/561 nm/638 nm; Chroma), and emission filters mounted in a filter wheel (525 nm/50 nm, 600 nm/50 nm; Chroma). Images were acquired every 10 seconds. The microscope system was controlled by NIS-Elements software (Nikon), and images were analyzed using FIJI/ImageJ (NIH). Microtubule plus and minus ends were identified by exhibiting dynamics parameters distinct to each end (see kymographs in Figure 2E for examples).

Anchorage independent growth assay

6-well dish (Eppendorf) was used for anchorage independent growth assay. 2ml of

autoclaved 1% agarose was used for bottom layer. After bottom layer became solid, 24 x 10^3 cells (MDAMB231 cells) were mixed into 2 ml of 0.8% agarose / media with or without CMPD1 or Taxol. After top layer gel became solid, cells were incubated in a humid atmosphere with 5% CO_2 for three weeks. 3 drops of complete media were supplied in each well every 3 days to avoid drying out. Cells were stained by 100 µg/ml of iodonitrotetrazolium chloride solution (Sigma) prior to taking photos.

Wound healing assay

H2B-mscarlet CAL-51 cells were plated in a 8-well chamber slide [what is the brand and catalog number of this chamber?]. 24 hours after cell seeding, a stripe of cell-free zone (the wound) was manually created on a highly confluent monolayer of cells using a sterile pipette tip. The cell culture media was then immediately replaced with a new one containing the indicated drugs (DMSO, 0.1, 0.5, 1, and 10 µM CMPD1). Then, the cell locomotion dynamics was monitored with live-cell imaging at an interval of 30 min. To quantify the cell migration efficiency in each condition, we used an ImageJ macro to measure the distance between two boundaries of the wound. Briefly, the two boundaries of the wound were drawn and defined manually. Then, 40 lines perpendicular to the two boundaries were drawn automatically and the length of each line was calculated and shown. The distance of cell movement was calculated by subtracting the distance at 20 hr post drug treatment from the original distance (0 hr). Each condition was normalized to the control.

Trans-well migration assay

CytoSelect 24-well cell invasion assay kits (Cell Biolabs) utilizing basement membrane-coated inserts were used according to the manufacturer's protocol. Briefly, cells treated with CMPD1 or DMSO were suspended in serum-free medium. Following overnight starvation, the cells were seeded at 3.0 × 104 cells/well in the upper chamber and incubated with the medium in the lower chamber for 48 hours. The invasive cells passing through the basement membrane layer were stained, and the absorbance of each well was measured at 560 nm after extraction.

Blood Invasion evaluation

All slides from mouse tumor with or without CMPD1 treatments were stained with HE and were screened for vascular invasion using strict criteria based on previous reports [72, 73]. All slides were blindly evaluated by two investigators (MT and HY). All these vascular invasions were adopted only if they were picked up on HE staining. Vascular invasion was identified by tumor cells within vessels. The cases were categorized as blood vessel invasion-positive or negative. Typical histologic pictures of blood vessel invasion positive and negative by HE staining are shown in Figure 5E.

RNA-seq

24 hours after 10 μM CMPD1 treatment, RNAs were purified by the RNeasy Mini Kit (Qiagen). Sequencing libraries were prepared with the TruSeq stranded mRNA kit and sequenced on NovaSeq6000 at Macrogen Japan. After adapter trimming, reads were mapped to the h38 human reference genome using STAR aligner[74]. Read counts for each gene were collected by featureCounts (version v1.6.4)[75]. Differentially expressed genes were identified with DESeq2[76] using filtering thresholds of FDR < 0.05. Pathway enrichment analysis was performed by DAVID[77].

Tumor xenograft

CB17-Prkdc^{scid}/Jcl mice were used for establishment of orthotopic breast cancer model and therapy. This mice strain was purchased from CLEA Japan, Inc. (Tokyo, Japan). Mice were maintained under specific pathogen-free conditions at the Chiba University. All experimental procedures were performed in strict accordance with the National Institute of Health guidelines and were approved by the Institutional Animal Care and Use Committee of Chiba University. For in vivo experiments, samples sizes were determined on the basis of knowledge of inter-tumor growth rate variability, gained from previous model-specific experience. MDA-MB-231 cells (1×10^6 cells / 0.1 ml) in 1:1 PBS: Matrigel were subcutaneously injected into the mammary fat pad of female mice. Tumors were allowed to develop for 30 days, and mice were then randomly assigned to each treatment groups, ensuring that baseline tumor volumes were balanced between treatment arms and treated

with CMPD1 (i.p., 15 μg/mouse/injection, 10 times for 3 weeks), Taxol (i.p., 5 mg/kg/injection, 10 times for 3 weeks). Both maximum and minimum diameters of the resulting tumors were measured every other day using a slide caliper. Tumor volumes were calculated as previously described. Mice were euthanized using CO2 inhalation. The maximum tumor diameter permitted under the relevant animal protocols is 25 mm, and this limit was not exceeded in any experiment.

FACS

MDA-MB-231 cells were incubated with present or absent of CMPD1 for 24 hours. Cells were then twice washed by PBS. Approximately 2 x 10^6 cells were fixed by ice cold Ethanol for 16 hours. Samples were washed by cold PBS, and stained by PI (Sigma) containing Triton-X (Sigma), and DNAse-free RNAse A (Sigma) in PBS for 30 min. Then samples were measured by a flow cytometer.

Statistics

Statistical significance was determined using two tailed unpaired student's t-test for comparison between two independent groups or one way ANOVA for multiped comparison. Two-tailed T-test was performed for Fig. 1C, 1G, 2A-B, 4A-B, 4E, and supplementary figs 4A, 4E-F, 6B-C, 6E, 7C-E. One way ANOVA (multiple comparison) was performed for figs 2H-I, 3B, 3D, 3G, 4D, 5B, 5F-G. For TIRF experiments in Figure 2 G-I, p values were

calculated from Z scores (2G; as previously described in Marzo et al., 2019; PMID 31364990), Mann–Whitney tests (2H-I, left and right), or by unpaired two-tailed Welch's t-tests (2H-I, middle). The latter two tests were selected as follows: the unpaired two-tailed Welch's t-test was used when the data sets were determined to be normal (by the D'Agostino and Pearson test for normality; $p > 0.05$). In the case where only one (or neither) was determined to be normal ($p < 0.05$), the Mann-Whitney test was used. For significance, * $p < 0.05$, ** $p < 0.01$, *** $p < 0.001$, **** $p < 0.0001$ were considered statistically significant. All quantifications were replicated at least two independent experiments.

Data availability

RNA-seq data generated in this study are available at Gene Expression Omnibus under Accession Number: GSE224462:

Go to https://www.ncbi.nlm.nih.gov/geo/query/acc.cgi?acc=GSE224462

Enter token: elwlcksijrqtzkx into the box

References

1. Hanahan, D. & Weinberg, R.A. Hallmarks of cancer: the next generation. *Cell* **144**, 646-674 (2011).

608 2. Aaronson, S.A. Growth factors and cancer. *Science* **254**, 1146-1153 (1991).
609 3. Chan, K.S., Koh, C.G. & Li, H.Y. Mitosis-targeted anti-cancer therapies: where they stand. *Cell Death Dis* **3**, e411
610 (2012).
611 4. Manchado, E., Guillamot, M. & Malumbres, M. Killing cells by targeting mitosis. *Cell Death Differ* **19**, 369-377
612 (2012).
613 5. Matson, D.R. & Stukenberg, P.T. Spindle poisons and cell fate: a tale of two pathways. *Mol Interv* **11**, 141-150
614 (2011).
615 6. Tischer, J. & Gergely, F. Anti-mitotic therapies in cancer. *J Cell Biol* **218**, 10-11 (2019).
616 7. Mukhtar, E., Adhami, V.M. & Mukhtar, H. Targeting microtubules by natural agents for cancer therapy. *Mol*
617 *Cancer Ther* **13**, 275-284 (2014).
618 8. Musacchio, A. The Molecular Biology of Spindle Assembly Checkpoint Signaling Dynamics. *Current biology : CB*
619 **25**, R1002-1018 (2015).
620 9. Lara-Gonzalez, P., Pines, J. & Desai, A. Spindle assembly checkpoint activation and silencing at kinetochores.
621 *Semin Cell Dev Biol* **117**, 86-98 (2021).
622 10. Musacchio, A. & Salmon, E.D. The spindle-assembly checkpoint in space and time. *Nature reviews. Molecular*
623 *cell biology* **8**, 379-393 (2007).
624 11. Jordan, M.A. Mechanism of action of antitumor drugs that interact with microtubules and tubulin. *Curr Med*
625 *Chem Anticancer Agents* **2**, 1-17 (2002).
626 12. Weaver, B.A. How Taxol/paclitaxel kills cancer cells. *Mol Biol Cell* **25**, 2677-2681 (2014).
627 13. Schiff, P.B., Fant, J. & Horwitz, S.B. Promotion of microtubule assembly in vitro by taxol. *Nature* **277**, 665-667
628 (1979).
629 14. Perez, E.A. Microtubule inhibitors: Differentiating tubulin-inhibiting agents based on mechanisms of action,
630 clinical activity, and resistance. *Mol Cancer Ther* **8**, 2086-2095 (2009).
631 15. Jordan, M.A. *et al.* The primary antimitotic mechanism of action of the synthetic halichondrin E7389 is
632 suppression of microtubule growth. *Mol Cancer Ther* **4**, 1086-1095 (2005).
633 16. Abu Samaan, T.M., Samec, M., Liskova, A., Kubatka, P. & Busselberg, D. Paclitaxel's Mechanistic and Clinical
634 Effects on Breast Cancer. *Biomolecules* **9** (2019).
635 17. Fountzilas, G. *et al.* A randomized phase III study comparing three anthracycline-free taxane-based regimens,
636 as first line chemotherapy, in metastatic breast cancer: a Hellenic Cooperative Oncology Group study. *Breast*
637 *Cancer Res Treat* **115**, 87-99 (2009).
638 18. Holmes, F.A. *et al.* Phase II trial of taxol, an active drug in the treatment of metastatic breast cancer. *J Natl*
639 *Cancer Inst* **83**, 1797-1805 (1991).
640 19. Kohn, E.C. *et al.* Dose-Intense Taxol: High Response Rate in Patients With Platinum-Resistant Recurrent Ovarian
641 Cancer. *JNCI Journal of the National Cancer Institute* **86**, 18-24 (1994).
642 20. Brewer, J.R., Morrison, G., Dolan, M.E. & Fleming, G.F. Chemotherapy-induced peripheral neuropathy: Current
643 status and progress. *Gynecol Oncol* **140**, 176-183 (2016).
644 21. Armstrong, D.K. *et al.* Intraperitoneal cisplatin and paclitaxel in ovarian cancer. *N Engl J Med* **354**, 34-43 (2006).
645 22. Banerji, A. *et al.* Management of hypersensitivity reactions to Carboplatin and Paclitaxel in an outpatient
646 oncology infusion center: a 5-year review. *J Allergy Clin Immunol Pract* **2**, 428-433 (2014).
647 23. Lipton, R.B. *et al.* Taxol produces a predominantly sensory neuropathy. *Neurology* **39**, 368-373 (1989).

648 24. Misawa, S. *et al.* Efficacy and safety of mirogabalin for chemotherapy-induced peripheral neuropathy: a
649 prospective single-arm trial (MiroCIP study). *BMC Cancer* **23**, 1098 (2023).
650 25. Kavallaris, M. *et al.* Taxol-resistant epithelial ovarian tumors are associated with altered expression of specific
651 beta-tubulin isotypes. *J Clin Invest* **100**, 1282-1293 (1997).
652 26. Kavallaris, M. Microtubules and resistance to tubulin-binding agents. *Nat Rev Cancer* **10**, 194-204 (2010).
653 27. Seve, P. & Dumontet, C. Is class III beta-tubulin a predictive factor in patients receiving tubulin-binding agents?
654 *Lancet Oncol* **9**, 168-175 (2008).
655 28. Eslamian, G., Wilson, C. & Young, R.J. Efficacy of eribulin in breast cancer: a short report on the emerging new
656 data. *Onco Targets Ther* **10**, 773-779 (2017).
657 29. Smith, J.A. *et al.* Eribulin binds at microtubule ends to a single site on tubulin to suppress dynamic instability.
658 *Biochemistry* **49**, 1331-1337 (2010).
659 30. O'Shaughnessy, J. *et al.* Impact of prior anthracycline or taxane use on eribulin effectiveness as first-line
660 treatment for metastatic breast cancer: results from two phase 2, multicenter, single-arm studies. *Springerplus*
661 **4**, 532 (2015).
662 31. Dumontet, C. & Jordan, M.A. Microtubule-binding agents: a dynamic field of cancer therapeutics. *Nat Rev Drug*
663 *Discov* **9**, 790-803 (2010).
664 32. Cortes, J. *et al.* Eribulin monotherapy versus treatment of physician's choice in patients with metastatic breast
665 cancer (EMBRACE): a phase 3 open-label randomised study. *The Lancet* **377**, 914-923 (2011).
666 33. Cortes, J. *et al.* Eribulin monotherapy versus treatment of physician's choice in patients with metastatic breast
667 cancer (EMBRACE): a phase 3 open-label randomised study. *Lancet* **377**, 914-923 (2011).
668 34. Cortes, J. *et al.* Phase II study of the halichondrin B analog eribulin mesylate in patients with locally advanced
669 or metastatic breast cancer previously treated with an anthracycline, a taxane, and capecitabine. *J Clin Oncol*
670 **28**, 3922-3928 (2010).
671 35. Wood, C.D., Thornton, T.M., Sabio, G., Davis, R.A. & Rincon, M. Nuclear localization of p38 MAPK in response to
672 DNA damage. *Int J Biol Sci* **5**, 428-437 (2009).
673 36. Borisova, M.E. *et al.* p38-MK2 signaling axis regulates RNA metabolism after UV-light-induced DNA damage.
674 *Nat Commun* **9**, 1017 (2018).
675 37. Yamashita, M. *et al.* TRAF6 mediates Smad-independent activation of JNK and p38 by TGF-beta. *Mol Cell* **31**,
676 918-924 (2008).
677 38. Han, J., Lee, J.D., Bibbs, L. & Ulevitch, R.J. A MAP kinase targeted by endotoxin and hyperosmolarity in
678 mammalian cells. *Science* **265**, 808-811 (1994).
679 39. Colomer, C. *et al.* IKKalpha Kinase Regulates the DNA Damage Response and Drives Chemo-resistance in Cancer.
680 *Mol Cell* **75**, 669-682 e665 (2019).
681 40. Arthur, J.S. & Ley, S.C. Mitogen-activated protein kinases in innate immunity. *Nat Rev Immunol* **13**, 679-692
682 (2013).
683 41. Segales, J., Perdiguero, E. & Munoz-Canoves, P. Regulation of Muscle Stem Cell Functions: A Focus on the p38
684 MAPK Signaling Pathway. *Front Cell Dev Biol* **4**, 91 (2016).
685 42. Canovas, B. & Nebreda, A.R. Diversity and versatility of p38 kinase signalling in health and disease. *Nat Rev Mol*
686 *Cell Biol* **22**, 346-366 (2021).
687 43. Cuadrado, A. & Nebreda, A.R. Mechanisms and functions of p38 MAPK signalling. *Biochem J* **429**, 403-417

688 (2010).
689 44. Young, P.R. Perspective on the discovery and scientific impact of p38 MAP kinase. *J Biomol Screen* **18**,
690 1156-1163 (2013).
691 45. Gurgis, F.M., Ziaziaris, W. & Munoz, L. Mitogen-activated protein kinase-activated protein kinase 2 in
692 neuroinflammation, heat shock protein 27 phosphorylation, and cell cycle: role and targeting. *Mol Pharmacol*
693 **85**, 345-356 (2014).
694 46. Yuan, J. *et al.* MAPK-activated protein kinase 2 is required for mouse meiotic spindle assembly and
695 kinetochore-microtubule attachment. *PLoS One* **5**, e11247 (2010).
696 47. Tang, J., Yang, X. & Liu, X. Phosphorylation of Plk1 at Ser326 regulates its functions during mitotic progression.
697 *Oncogene* **27**, 6635-6645 (2008).
698 48. Davidson, W. *et al.* Discovery and characterization of a substrate selective p38alpha inhibitor. *Biochemistry* **43**,
699 11658-11671 (2004).
700 49. Mamidi, P. *et al.* MK2a inhibitor CMPD1 abrogates chikungunya virus infection by modulating actin remodeling
701 pathway. *PLoS Pathog* **17**, e1009667 (2021).
702 50. Wu, Y. *et al.* MK2 mediates macrophage activation and acute lung injury by regulating let-7e miRNA. *Am J*
703 *Physiol Lung Cell Mol Physiol* **315**, L371-L381 (2018).
704 51. Hendriks, B.S., Seidl, K.M. & Chabot, J.R. Two additive mechanisms impair the differentiation of
705 'substrate-selective' p38 inhibitors from classical p38 inhibitors in vitro. *BMC Syst Biol* **4**, 23 (2010).
706 52. Li, Y. *et al.* CMPD1 inhibited human gastric cancer cell proliferation by inducing apoptosis and G2/M cell cycle
707 arrest. *Biol Res* **51**, 11 (2018).
708 53. Gurgis, F. *et al.* Cytotoxic activity of the MK2 inhibitor CMPD1 in glioblastoma cells is independent of MK2. *Cell*
709 *Death Discov* **1**, 15028 (2015).
710 54. Jordan, M.A. & Wilson, L. Microtubules as a target for anticancer drugs. *Nat Rev Cancer* **4**, 253-265 (2004).
711 55. Moudi, M., Go, R., Yien, C.Y. & Nazre, M. Vinca alkaloids. *Int J Prev Med* **4**, 1231-1235 (2013).
712 56. Dai, X., Cheng, H., Bai, Z. & Li, J. Breast Cancer Cell Line Classification and Its Relevance with Breast Tumor
713 Subtyping. *J Cancer* **8**, 3131-3141 (2017).
714 57. Neve, R.M. *et al.* A collection of breast cancer cell lines for the study of functionally distinct cancer subtypes.
715 *Cancer Cell* **10**, 515-527 (2006).
716 58. Huovinen, M., Loikkanen, J., Myllynen, P. & Vahakangas, K.H. Characterization of human breast cancer cell lines
717 for the studies on p53 in chemical carcinogenesis. *Toxicol In Vitro* **25**, 1007-1017 (2011).
718 59. Tentler, J.J. *et al.* p53 Family Members Regulate Phenotypic Response to Aurora Kinase A Inhibition in
719 Triple-Negative Breast Cancer. *Mol Cancer Ther* **14**, 1117-1129 (2015).
720 60. Scribano, C.M. *et al.* Chromosomal instability sensitizes patient breast tumors to multipolar divisions induced
721 by paclitaxel. *Sci Transl Med* **13**, eabd4811 (2021).
722 61. Vasiliev, J.M. *et al.* Effect of colcemid on the locomotory behaviour of fibroblasts. *J Embryol Exp Morphol* **24**,
723 625-640 (1970).
724 62. Liao, G., Nagasaki, T. & Gundersen, G.G. Low concentrations of nocodazole interfere with fibroblast locomotion
725 without significantly affecting microtubule level: implications for the role of dynamic microtubules in cell
726 locomotion. *J Cell Sci* **108 (Pt 11)**, 3473-3483 (1995).
727 63. Etienne-Manneville, S. Microtubules in cell migration. *Annu Rev Cell Dev Biol* **29**, 471-499 (2013).

728 64. Guo, M. *et al.* Targeting MK2 Is a Novel Approach to Interfere in Multiple Myeloma. *Front Oncol* **9**, 722 (2019).
729 65. Gu, C. *et al.* MK2 is a therapeutic target for high-risk multiple myeloma. *Haematologica* **106**, 1774-1777 (2021).
730 66. Berggren, K.L. *et al.* MAPKAPK2 (MK2) inhibition mediates radiation-induced inflammatory cytokine
731 production and tumor growth in head and neck squamous cell carcinoma. *Oncogene* **38**, 7329-7341 (2019).
732 67. Kudaravalli, S., den Hollander, P. & Mani, S.A. Role of p38 MAP kinase in cancer stem cells and metastasis.
733 *Oncogene* **41**, 3177-3185 (2022).
734 68. Morgan, D. *et al.* Mitogen-activated protein kinase-activated protein kinase-2 (MK2) and its role in cell survival,
735 inflammatory signaling, and migration in promoting cancer. *Mol Carcinog* **61**, 173-199 (2022).
736 69. Pomerance, M., Quillard, J., Chantoux, F., Young, J. & Blondeau, J.P. High-level expression, activation, and
737 subcellular localization of p38-MAP kinase in thyroid neoplasms. *J Pathol* **209**, 298-306 (2006).
738 70. Suresh, K. *et al.* Tumor MK2 transcript levels are associated with improved response to chemotherapy and
739 patient survival in non-small cell lung cancer. *Physiol Genomics* **55**, 168-178 (2023).
740 71. Suzuki, A., Badger, B.L. & Salmon, E.D. A quantitative description of Ndc80 complex linkage to human
741 kinetochores. *Nature communications* **6**, 8161 (2015).
742 72. Pinder, S.E. *et al.* Pathological prognostic factors in breast cancer. III. Vascular invasion: relationship with
743 recurrence and survival in a large study with long-term follow-up. *Histopathology* **24**, 41-47 (1994).
744 73. Lauria, R. *et al.* The prognostic value of lymphatic and blood vessel invasion in operable breast cancer. *Cancer*
745 **76**, 1772-1778 (1995).
746 74. Dobin, A. *et al.* STAR: ultrafast universal RNA-seq aligner. *Bioinformatics* **29**, 15-21 (2013).
747 75. Liao, Y., Smyth, G.K. & Shi, W. featureCounts: an efficient general purpose program for assigning sequence
748 reads to genomic features. *Bioinformatics* **30**, 923-930 (2013).
749 76. Love, M.I., Huber, W. & Anders, S. Moderated estimation of fold change and dispersion for RNA-seq data with
750 DESeq2. *Genome Biology* **15** (2014).
751 77. Huang, D.W., Sherman, B.T. & Lempicki, R.A. Systematic and integrative analysis of large gene lists using DAVID
752 bioinformatics resources. *Nature protocols* **4**, 44-57 (2008).
753
754
755
756
757
758
759
760
761
762
763
764
765
766
767

Legends

Figure 1. CMPD1 induced severe mitotic arrest in multiple cancer cell lines

(A) Chemical structure of CMPD1. (B) FACS analysis of MDA-MB-231 cells treated with DMSO or 1, 5, or 10 μM CMPD1 for 24 hours. (C) Representative time-lapse images of MDA-MB-231, CAL-51, and T-47D cells treated with either DMSO or 5 μM CMPD1. Time is indicated in minutes post-NEBD. (D) Quantification of mitotic duration of MDA-MB-231, CAL-51, and T-47D treated with DMSO, 1, 5, or 10 μM CMPD1. n = 30-60 cells pooled from two independent replicates. Error bars are mean ± s.d. Asterisk above each dot plot indicates the significant difference ($p < 0.0001$, Tukey's multiple comparison test) between the indicated drug-treated condition and the control.

Figure 2. CMPD1 treatment specifically attenuates mitotic fidelity of cancer cells

(A) Representative time-lapse images (interval: 3 min) of RPE1, MDA-MB-231, and CAL-51 cells treated with DMSO or low dose of CMPD1 (10 and 50 nM). All of these three cell lines express H2B-GFP. Time is indicated in minutes post-NEBD. (B) Quantification of

mitotic duration of cells shown in (A). n = 70, 60, 60, 60, 60, 65, 50, 84, 101 cells from left to right. (C) The enlarged plot of a red box region shown in (B). (D) Representative images of mitotic defects. Note that “misaligned” and “no metaphase plate” were annotated only when the cells exhibited this phenotype upon anaphase onset. (E) Normalized percentage of mitotic cells exhibiting accurate chromosome segregation in each condition. The data derived from CMPD1-treated cells were normalized to the data derived from DMSO-treated cells for each cell line. (F) Left: representative time-lapse images (interval: 3 min) of untreated RPE1 cells, and RPE1, MDA-MB-231, and CAL-51 cells treated with 10 nM PTX. Right: The quantification of the fraction of mitotic cells showing mitotic errors. The p-value was calculated by Tukey's multiple comparisons test. Time is indicated in minutes post-washout. (G) Representative images of RPE1, MDA-MB-231, and CAL-51 cells in CMPD1 washout experiments. Briefly, cells were treated with 2 μM CMPD1 for 4 hours, followed by a wash with complete media and live-cell imaging. Time is indicated in minutes post-washout. (H) The mitotic duration of mitotic cells that were arrested by CMPD1 in the beginning of the imaging. The mitotic duration was defined as the time from the start of the imaging to anaphase onset or mitotic exit. The mean value was shown at the top right of each condition. n = 54, 60, and 37 cells for RPE1, MDA-MB-231, and CAL-51 cells, respectively. The p-value was calculated by Tukey's multiple comparisons test. (I) Quantification of the percentage of mitotic cells showing normal chromosome segregation. The mean value was shown at the top right of each condition. n = 50 cells in each condition

pooled from two independent experiments. The p-value was calculated by Tukey's multiple comparisons test. Error bars are mean ± s.d.

Figure 3. CMPD1 inhibits both anchorage independent growth and tumor growth in mice

(A) Representative images of anchorage independent growth assay using MDA-MB-231 cells treated with DMSO, CMPD1 at different conditions (0.01, 0.05, 0.1, 0.25, 0.5, and 1 μM), or 10 μM PTX. (B) The normalized number of cell colonies formed in each condition. Error bars are mean ± s.d. Three independent experiments were performed for each condition. (C) Schematic diagram of the mouse xenograft experiment and the drug treatment schedule. (D) The image of tumors in each condition at the time of necropsy. The tumors were arranged in order based on their size. (E) The quantification of gross weight of tumors at the time of necropsy. Error bars are mean ± s.d.

Figure 4. CMPD1 induces microtubule depolymerization

(A) Representative time-lapse images of CAL-51 cells expressing α-Tubulin-mNeonGreen and H2B-mScalret upon the treatment with DMSO, 2 μM CMPD1, or 10 μM MG132 along with 2 μM CMPD1. CMPD1 was added into the cell culture media immediately after images at the first time point were acquired. Time is indicated in minutes. (B) The quantification of the signal levels of mitotic spindles over time in each condition shown in (A). (C)

Representative time-lapse images (interval: 2 min) of a G2 phase CAL-51 cell expressing α-Tubulin-mNeonGreen and H2B-mScarlet in the presence of 2 μM CMPD1. Note that the two bright dots in the Tubulin channel indicate the two clustered centrosomes before NEBD. The arrow in the DNA channel indicates the time of NEBD. Time is indicated in minutes. (D) Representative kymographs depicting microtubule plus and minus end dynamics before and after the addition of polymerization mix supplement with 15 μM tubulin alone, or 15 μM tubulin supplemented with either 20 μM CMPD1 or 5 μM vinblastine, as indicated (GMPCPP-stabilized microtubule seeds, magenta; microtubules polymerized from seeds, green; see Methods). Plus ends are positioned to the right, and minus ends are positioned to the left of the seeds in all kymographs. Arrows indicate the time of addition of tubulin alone, or tubulin plus drug. (E) Plot depicting fraction of microtubules with detectable plus or minus ends 1 minute after addition of drug, or tubulin alone (n = 27, 29, and 30 microtubules from left to right). Error bars indicate mean ± s.d. (F) Representative images from a time-lapse sequence showing microtubule plus and minus end lengths 10 seconds prior to, and 5 and 15 seconds after addition of polymerization mix supplemented with 20 μM CMPD1. (G) Plots depicting plus end catastrophe frequencies (n = 51 and 41 microtubules from left to right), plus end growth rates (n = 172 and 91 events from left to right), and normalized maximum length (n = 55 and 41 microtubules from left to right) achieved over the imaging period. (H) Plots depicting minus end catastrophe frequencies (n = 51 and 41 microtubules from left to right), minus end growth rates (n = 129 and 63 events

from left to right), and normalized maximum length (n = 55 and 40 microtubules from left to right) achieved over the imaging period. Error bars indicate mean ± s.d. Data were pooled from at least 2-4 independent replicates (G-H).

Figure 5. CMPD1 inhibits cancer cell migration and invasion

(A) Representative images of H2B-mScarlet CAL-51 cells treated with DMSO, or CMPD1 at different concentrations (0, 0.1, 0.5, 1, 10 μM) at three different time points (0, 24, and 48 hr post-treatment). A wound (cell-free zone) was created using a tip, followed by the addition of indicated drugs and live-cell imaging (interval: 30 min). (B) Quantification of cell migration speed when cells were treated with indicated drugs. Each condition was normalized to the speed of DMSO-treated cells. The distance between the edge of the wound was measured using imageJ macro. Results are the mean ± s.d. N = 3 biological replicates. (C) Representative images of trans-well invasion assay using MDA-MB-231 cells treated with DMSO, CMPD1 (0.1, 1, 2, 5 μM), or 10 μM PTX. (D) The quantification of the average number of invaded cells in each condition shown in (C). (E) Left: example images of blood vessels in xenograft tumors derived from mice treated with DMSO or 1.0 mg/kg CMPD1 as shown in Fig. 3C. Two sets of example images acquired from different tumors were shown. Right: the quantification of the percentage of blood vessels infiltrated with cancer cells. Error bars are mean ± s.d.

Figure 6. MK2 inhibition enhances the efficacy of microtubule inhibitors in cancer cells

(A) Left: representative time-lapse images of mitotic CAL-51 cells treated with indicated combinations of drugs (10 μM MK2i, 1 nM vinblastine, 5 nM vinblastine). Right: quantification of the mitotic duration, mitotic error rate, mitotic slippage rate, and the frequency of death in mitosis. The fate of mitotic cells was color-coded. N = 100 cells pooled from two biological replicates for each condition. Time is indicated in minutes post-NEBD. (B) Volcano plot displaying changes in gene expression following CMPD1 treatment in MDA-MB-231 cells. RNA-seq was conducted with three biological replicates. Differentially expressed genes (DEGs) are highlighted in red (up-regulated) and blue (down-regulated). (C) Pathway enrichment analysis of differentially expressed genes using the Gene Ontology (GO) Biological Processes (BP). Enrichment analysis was performed with the DAVID online tool. (D) Comparison of GO Biological Process enrichment analysis of DEGs unique to MDA-MB-231 cells relative to RPE1 cells. Genes uniquely up- or down-regulated in MDA-MB-231 cells, but not in RPE1 cells, were subjected to GO BP enrichment analysis.

Figure 7. The model of CMPD1-mediated cytotoxicity effects on cancer cells.

CMPD1 exhibits its tumor-specific cytotoxicity likely via two pathways. First, CMPD1 acts as a kinase inhibitor which prevents p38 MAPK-dependent phosphorylation of MK2,

leading to the disruption of proper actin remodeling and spindle formation during mitosis. Second, CMPD1 serves as a MTA which can specifically induce depolymerization at the plus ends of microtubules. Both impaired actin reorganization and attenuated microtubule filament formation inhibit cancer cell migration and invasion, thereby preventing metastasis. On the other hand, failure of spindle assembly during mitosis causes the extended prometaphase arrest and the diminished mitotic fidelity, resulting in apoptosis of tumor cells and tumor shrinkage.

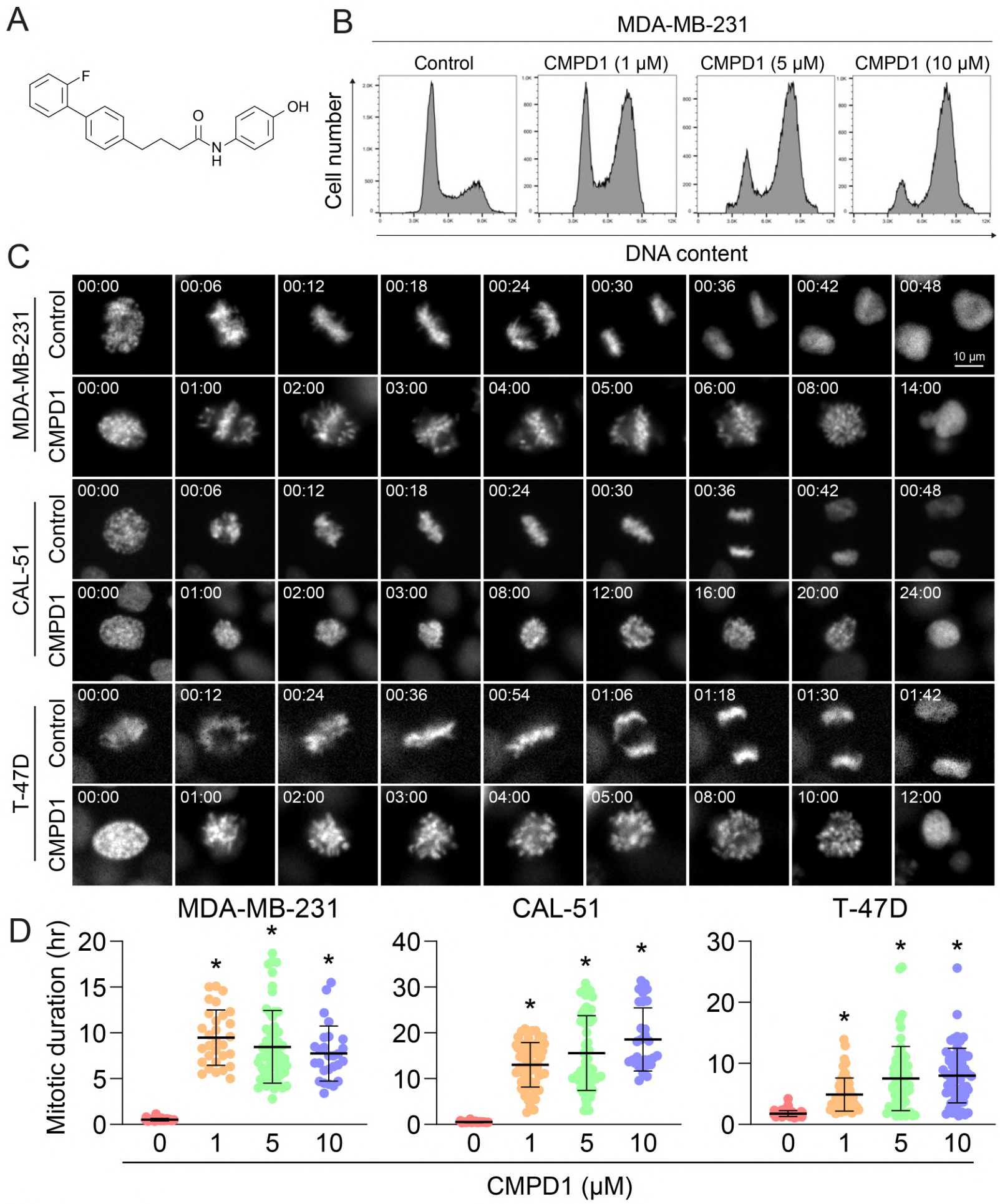
A
F
O
OH
N
H
B
MDA-MB-231
Control
CMPD1 (1 μM)
CMPD1 (5 μM)
CMPD1 (10 μM)
Cell number
DNA content
C
MDA-MB-231
Control
CMPD1
CAL-51
Control
CMPD1
T-47D
Control
CMPD1
10 μm
D
MDA-MB-231
CAL-51
T-47D
Mitotic duration (hr)
CMPD1 (μM)

Figure 1

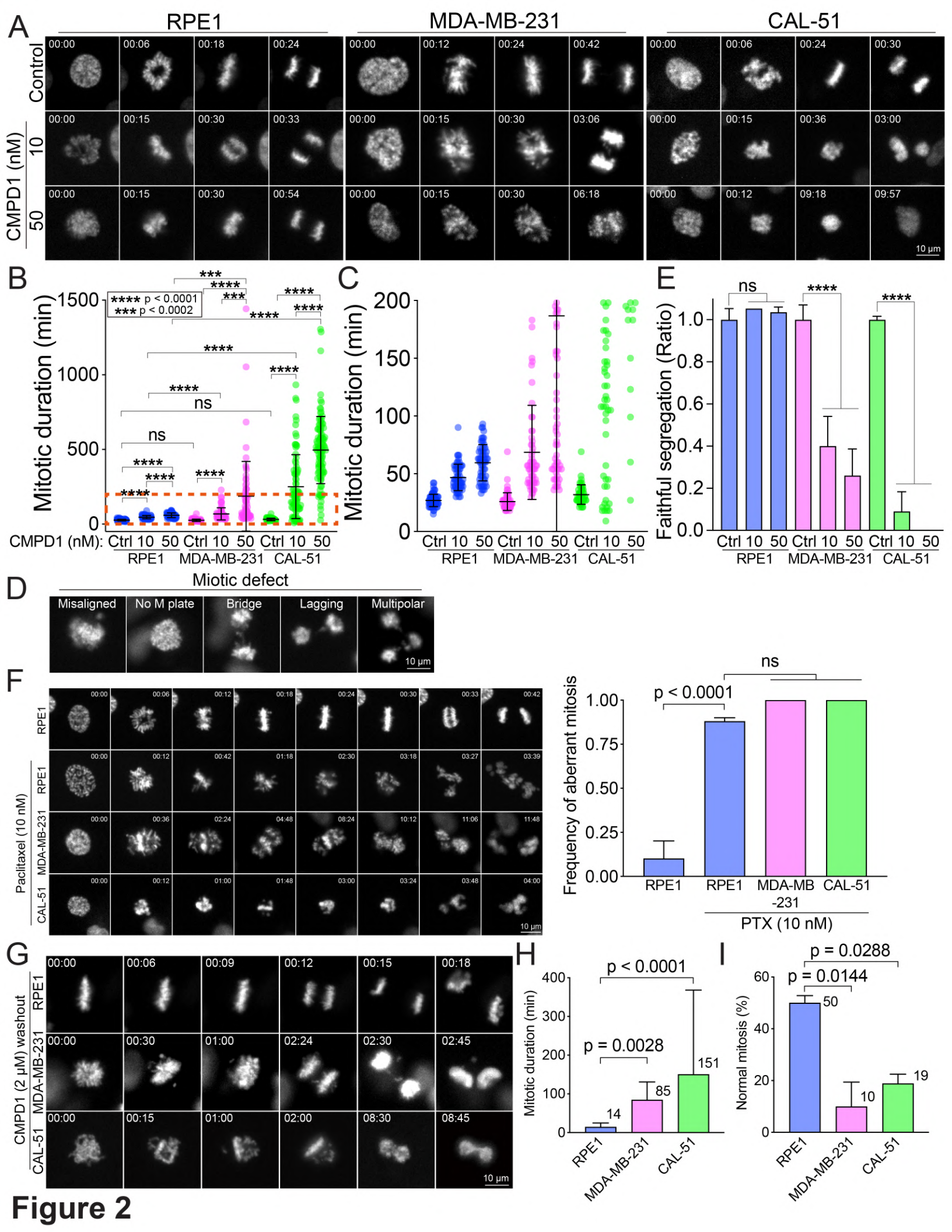
A
RPE1
MDA-MB-231
CAL-51
Control
CMPD1 (nM)
10
50
10 µm
B
Mitotic duration (min)
**** p < 0.0001
*** p < 0.0002
ns
CMPD1 (nM): Ctrl 10 50 Ctrl 10 50 Ctrl 10 50
RPE1 MDA-MB-231 CAL-51
C
Mitotic duration (min)
Ctrl 10 50 Ctrl 10 50 Ctrl 10 50
RPE1 MDA-MB-231 CAL-51
E
Faithful segregation (Ratio)
ns
****
Ctrl 10 50 Ctrl 10 50 Ctrl 10 50
RPE1 MDA-MB-231 CAL-51
D
Miotic defect
Misaligned
No M plate
Bridge
Lagging
Multipolar
10 µm
F
Paclitaxel (10 nM)
RPE1
MDA-MB-231
CAL-51
10 µm
Frequency of aberrant mitosis
ns
p < 0.0001
RPE1
RPE1
MDA-MB -231
CAL-51
PTX (10 nM)
G
CMPD1 (2 µM) washout
RPE1
MDA-MB-231
CAL-51
10 µm
H
Mitotic duration (min)
p < 0.0001
p = 0.0028
14
85
151
RPE1
MDA-MB-231
CAL-51
I
Normal mitosis (%)
p = 0.0288
p = 0.0144
50
10
19
RPE1
MDA-MB-231
CAL-51

Figure 2

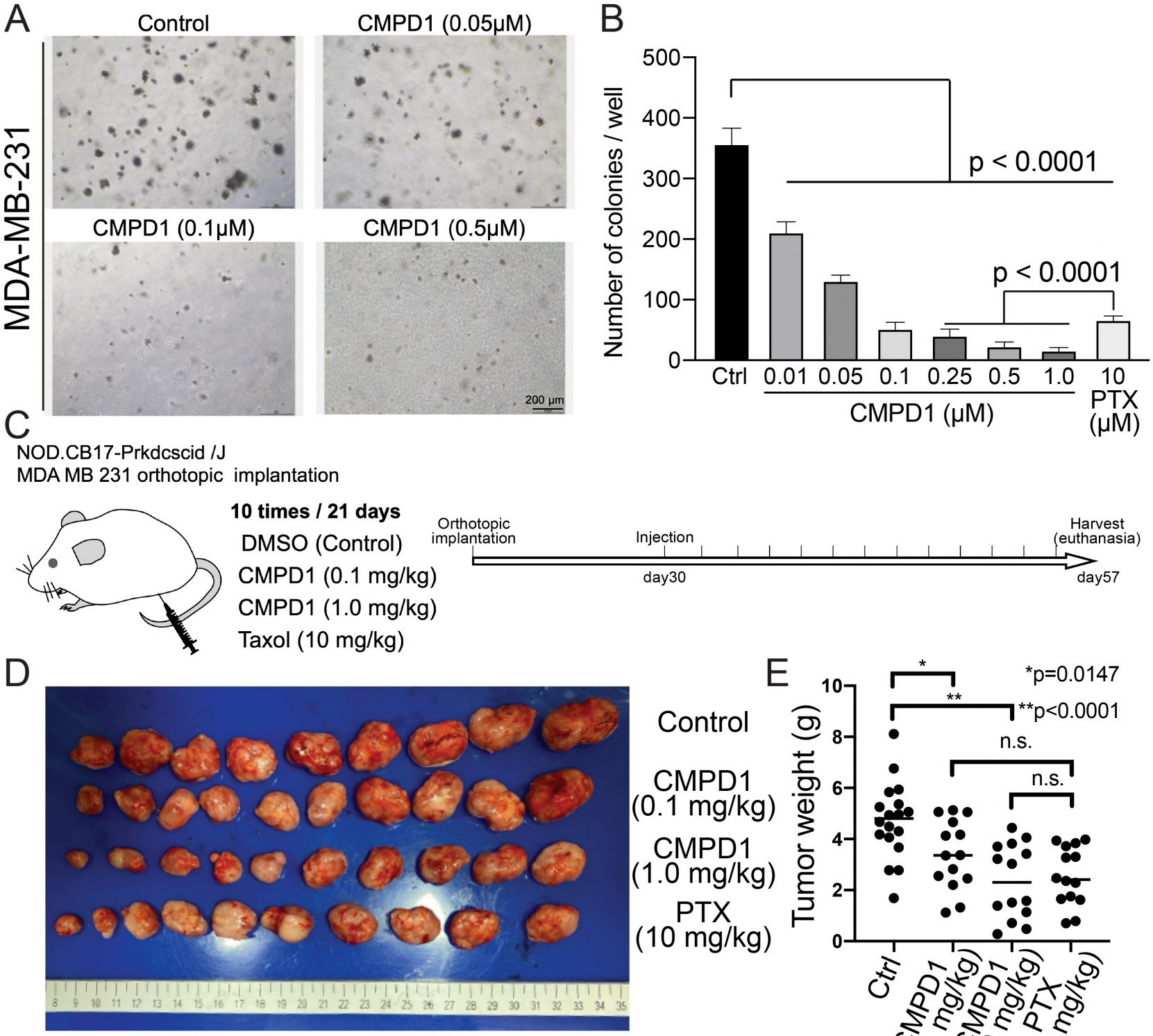
A
Control
CMPD1 (0.05μM)
MDA-MB-231
CMPD1 (0.1μM)
CMPD1 (0.5μM)
200 μm
B
Number of colonies / well
500
400
300
200
100
0
p < 0.0001
p < 0.0001
Ctrl
0.01
0.05
0.1
0.25
0.5
1.0
10
CMPD1 (μM)
PTX (μM)
C
NOD.CB17-Prkdcscid /J
MDA MB 231 orthotopic implantation
10 times / 21 days
DMSO (Control)
CMPD1 (0.1 mg/kg)
CMPD1 (1.0 mg/kg)
Taxol (10 mg/kg)
Orthotopic implantation
Injection
Harvest (euthanasia)
day30
day57
D
Control
CMPD1 (0.1 mg/kg)
CMPD1 (1.0 mg/kg)
PTX (10 mg/kg)
E
*p=0.0147
**p<0.0001
n.s.
n.s.
Tumor weight (g)
10
8
6
4
2
0
Ctrl
CMPD1 (0.1 mg/kg)
CMPD1 (1.0 mg/kg)
PTX (10 mg/kg)

Figure 3

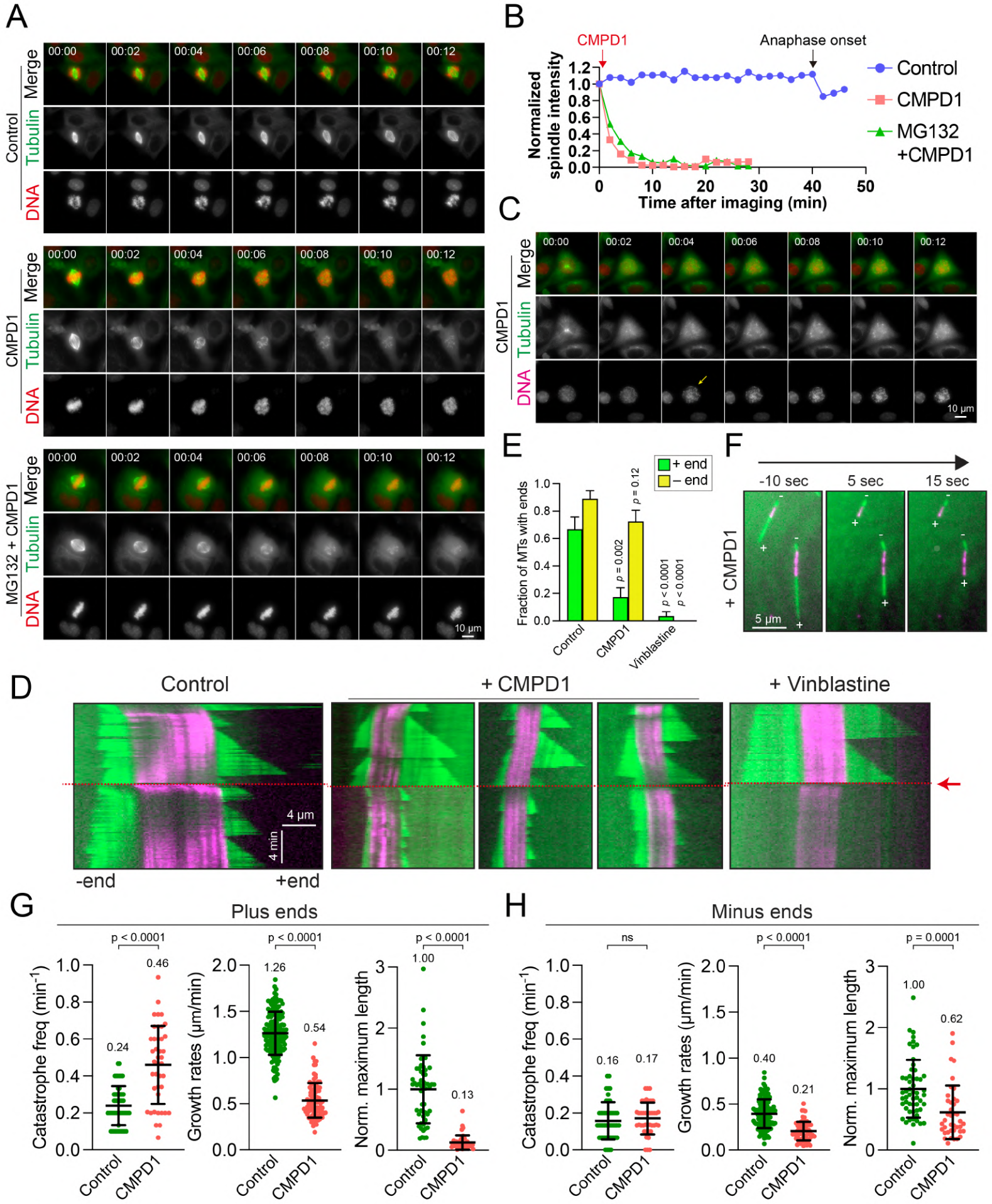
A
Control
CMPD1
MG132 + CMPD1
Merge
Tubulin
DNA
00:00
00:02
00:04
00:06
00:08
00:10
00:12
10 µm
B
CMPD1
Anaphase onset
Normalized spindle intensity
Time after imaging (min)
Control
CMPD1
MG132 +CMPD1
C
D
Control
+ CMPD1
+ Vinblastine
4 µm
4 min
-end
+end
E
Fraction of MTs with ends
+ end
– end
p = 0.002
p = 0.12
p < 0.0001
p < 0.0001
Control
CMPD1
Vinblastine
F
-10 sec
5 sec
15 sec
+ CMPD1
5 µm
G
Plus ends
Catastrophe freq (min-1)
Growth rates (µm/min)
Norm. maximum length
p < 0.0001
0.24
0.46
1.26
0.54
1.00
0.13
H
Minus ends
ns
p < 0.0001
p = 0.0001
0.16
0.17
0.40
0.21
1.00
0.62

Figure 4

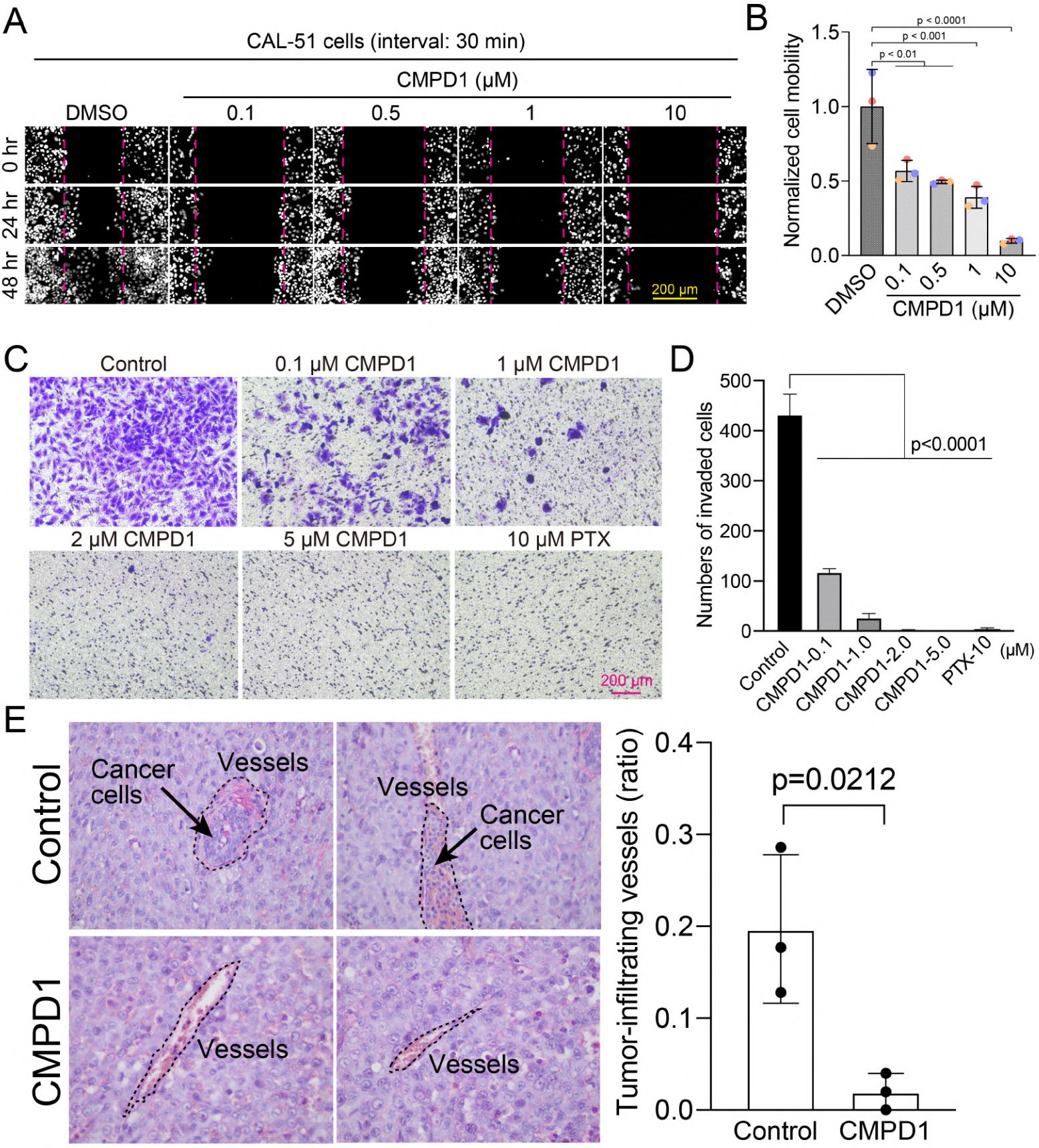
A
CAL-51 cells (interval: 30 min)
CMPD1 (μM)
DMSO
0.1
0.5
1
10
0 hr
24 hr
48 hr
200 μm
B
Normalized cell mobility
p < 0.0001
p < 0.001
p < 0.01
DMSO
0.1
0.5
1
10
CMPD1 (μM)
C
Control
0.1 μM CMPD1
1 μM CMPD1
2 μM CMPD1
5 μM CMPD1
10 μM PTX
200 μm
D
Numbers of invaded cells
p<0.0001
Control
CMPD1-0.1
CMPD1-1.0
CMPD1-2.0
CMPD1-5.0
PTX-10
(μM)
E
Control
CMPD1
Cancer cells
Vessels
Tumor-infiltrating vessels (ratio)
p=0.0212
Control
CMPD1

Figure 5

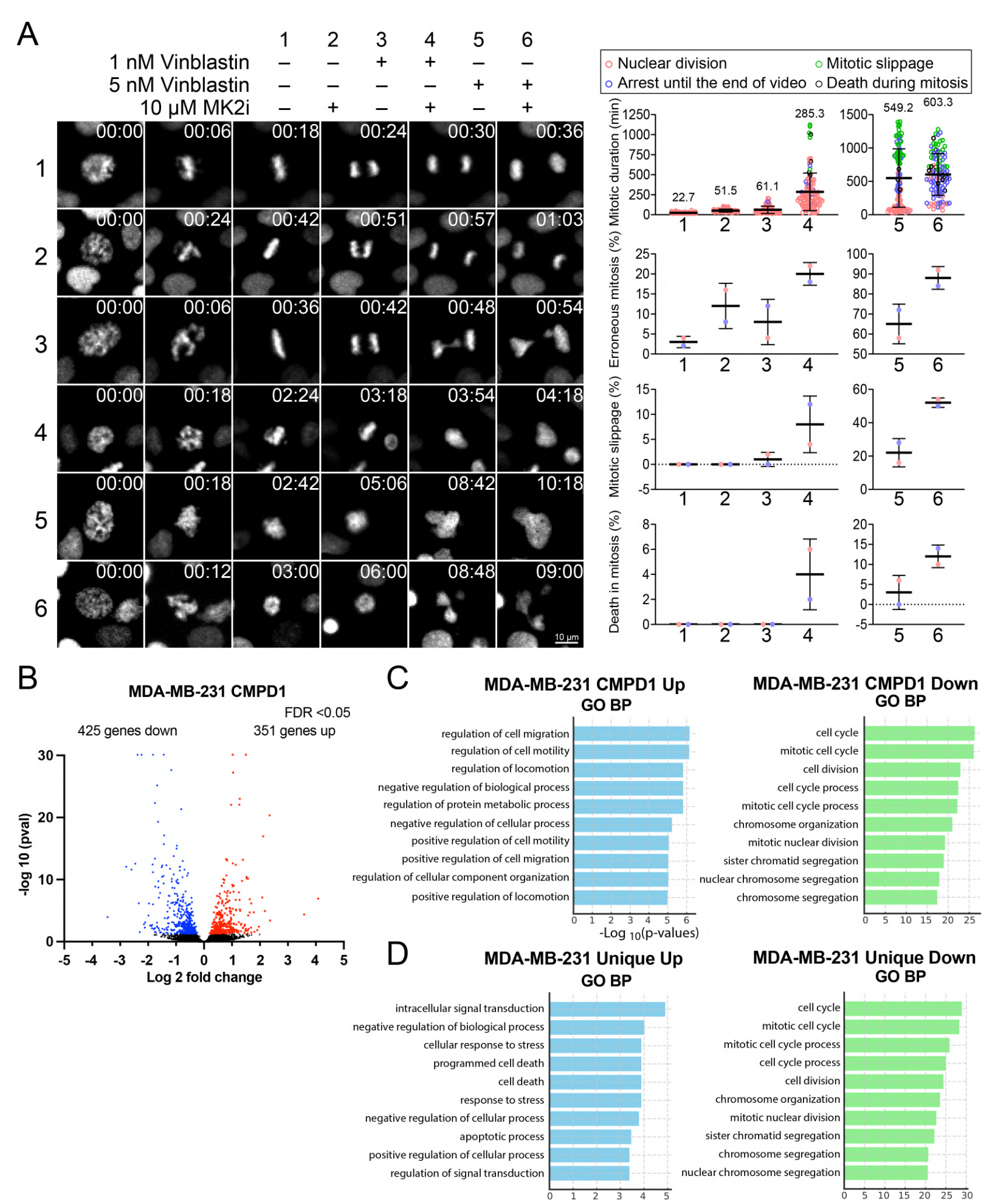
A
1 2 3 4 5 6
1 nM Vinblastin – – + + – –
5 nM Vinblastin – – – – + +
10 μM MK2i – + – + – +
00:00 00:06 00:18 00:24 00:30 00:36
00:00 00:24 00:42 00:51 00:57 01:03
00:00 00:06 00:36 00:42 00:48 00:54
00:00 00:18 02:24 03:18 03:54 04:18
00:00 00:18 02:42 05:06 08:42 10:18
00:00 00:12 03:00 06:00 08:48 09:00
10 μm
Nuclear division
Mitotic slippage
Arrest until the end of video
Death during mitosis
Mitotic duration (min)
22.7
51.5
61.1
285.3
549.2
603.3
Erroneous mitosis (%)
Mitotic slippage (%)
Death in mitosis (%)
B
MDA-MB-231 CMPD1
FDR <0.05
425 genes down
351 genes up
-log 10 (pval)
Log 2 fold change
C
MDA-MB-231 CMPD1 Up
GO BP
regulation of cell migration
regulation of cell motility
regulation of locomotion
negative regulation of biological process
regulation of protein metabolic process
negative regulation of cellular process
positive regulation of cell motility
positive regulation of cell migration
regulation of cellular component organization
positive regulation of locomotion
-Log 10(p-values)
MDA-MB-231 CMPD1 Down
GO BP
cell cycle
mitotic cell cycle
cell division
cell cycle process
mitotic cell cycle process
chromosome organization
mitotic nuclear division
sister chromatid segregation
nuclear chromosome segregation
chromosome segregation
D
MDA-MB-231 Unique Up
GO BP
intracellular signal transduction
negative regulation of biological process
cellular response to stress
programmed cell death
cell death
response to stress
negative regulation of cellular process
apoptotic process
positive regulation of cellular process
regulation of signal transduction
MDA-MB-231 Unique Down
GO BP
cell cycle
mitotic cell cycle
mitotic cell cycle process
cell cycle process
cell division
chromosome organization
mitotic nuclear division
sister chromatid segregation
chromosome segregation
nuclear chromosome segregation

Figure 6

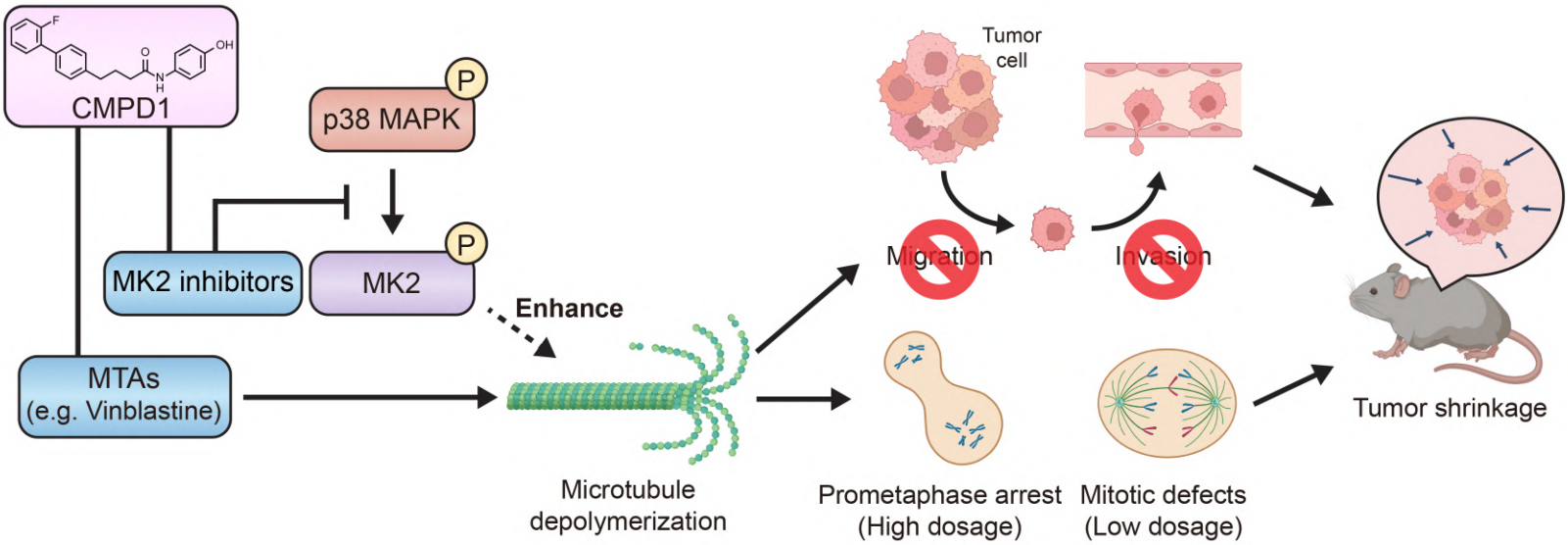
CMPD1
p38 MAPK
P
MK2 inhibitors
MK2
P
Enhance
MTAs
(e.g. Vinblastine)
Microtubule
depolymerization
Tumor
cell
Migration
Invasion
Prometaphase arrest
(High dosage)
Mitotic defects
(Low dosage)
Tumor shrinkage

Figure 7